Advanced space-charge-limited current model for analyzing fermi level shift in the bandgap of halide perovskites

Check for updates

Stevan Gavranovic ⬤ ✉, Oldrich Zmeskal, Martin Weiter & Jan Pospisil ⬤ ✉

Understanding how charge carriers behave in semiconductors is key to improving next-generation optoelectronic devices. Here we introduce an advanced space-charge-limited current model that enables detailed extraction of mobility, charge carrier concentrations, and Fermi level position from voltage- and energy-dependent analysis. Applying this model to two promising halide perovskites, methylammonium lead bromide and methylammonium lead iodide, we observe a strong photoresponse, with significant increases in microscopic mobility and free carrier density under illumination. Interestingly, the behavior of trapped charges and Fermi level shifts differs between the two materials, revealing distinct transport mechanisms. This model offers a powerful tool for characterizing semiconductors and could accelerate the development of more efficient light-sensitive devices.

The rapid increase in power conversion efficiency, from 3.8% (2009)[1] to 26.1% (2023)[2], reported in halide perovskites solar cells (PSCs), has started a new generation of photovoltaics and put these materials in the focus of optoelectronic research. Their unique properties (high absorption coefficient[3–5], tunable bandgap[6–8], long range carrier mobilities[3,9–12], and low defect density[13–15] opened a broad spectrum of possible applications such as solar cells[16–21], photodetectors[15,22–26], field-effect transistors[27–30], light emitting diodes[31–34], memristors[35,36], and lasers[37–40]. Organometal halide perovskites typically come in the form of organic-inorganic crystalline compounds with the general formula of $APbX_3$[41], where A is a monovalent cation (methylammonium, MA^+, formamidinium FA^+ or cesium Cs^+), and X is a halide anion (chloride Cl^-, bromide Br^- and iodide I^-).

Interestingly, their key optoelectronic properties, such as optical bandgap, can be easily tailored by chemical engineering before the synthesis of these solution-processable materials. For example, the bathochromic shift, that is the decrease of optical bandgap reported in $MAPbX_3$, occurs when chloride (2.97 eV) is substituted with larger halide anions, bromide (2.22 eV) or iodide (1.50 eV)[42]. Other important factors in future practical applications are represented by the charge carrier transport and defect density, both of which are highly dependent on the type of the perovskite active layer. It has been widely accepted that perovskite single crystals exhibit significantly better charge transport properties compared to those of their polycrystalline thin film counterparts. The bulk perovskite single crystals show long periodicity of crystalline lattice and very low density of trap states $(2–200 \times 10^9 \, cm^{-3})$[43,44]. On the contrary, multiple grain boundaries in polycrystalline thin films create deep trap states (trap density $\approx 1 \times 10^{17} \, cm^{-3})$[45], and they also promote the electron-hole recombination;

hence, they decrease the effectivity of charge carrier transport. Thus, single crystals make a good platform to explore the intrinsic properties of organometal halide perovskites.

Although extensive research has been performed, there is a lack of unanimous experimental and modeling procedures to determine both the charge carrier mobilities and concentration of trapped charge carriers in organometal halide perovskite. To determine the above parameters, the space-charge limited current (SCLC) method is commonly used. Essentially, this method is based on the complex analysis of current-voltage characteristics (also known as the *J-V* curves) of semiconductor materials with trap states. It identifies and distinguishes the three regions present in *J-V* curves: (1) ohmic region (i.e. the slope of current-voltage characteristic is equal to one); (2) trap filing region (the slope is greater than 2); and (3) quadratic region (the slope is equal to 2, i.e. the monoenergetic trap state or Mott–Gurney region).

However, this method has multiple shortcomings that may lead to underestimation and inaccurate interpretation of *J-V* characteristics. Firstly, commonly applied approaches use tangent fitting[44–49] to identify the different regions of *J-V* characteristics and estimate the electric properties of the perovskite materials (mainly charge carrier mobility and concentration of the trapped states). Secondly, the halide perovskite materials are known for their electronic and ionic nature[50–52], which affect the *J-V* characteristics and complicate their analysis and interpretation. Many efforts have been put toward understanding of ionic processes and their effects on *J-V* hysteresis and SCLC parameters. Duijnstee et al.[53] and Le Corre et al.[54] developed complex experimental and modeling approach to describe the ionic effects on the measured *J-V* characteristics

Faculty of Chemistry, Brno University of Technology, Purkynova, Brno, Czech Republic. ✉e-mail: xcgavranovic@vutbr.cz; pospisilj@fch.vut.cz

and quantify the concentrations of ions using drift diffusion model. In a recent SCLC analysis of MAPbI$_3$-based devices Sajedi Alvar, et al.[55] demonstrate the importance of temperature-dependent ion dynamics and temperature- and frequency-dependent dielectric constants. The authors suggest that only experimentally validated parameters should be used to build the SCLC model. Though the latest SCLC modeling approach enabled precise simulation of J-V curves and determination of ion influence on the shape of the characteristics, some of the fundamental properties describing the charge dynamics (e.g. energy and voltage dependance of modeled parameters) are still not described in detail.

Herein, we report a modeling approach to determine the energetic distribution of the charge carrier (electron and holes) mobilities, of trapped state density, and of Fermi level using advanced space charge limited current (A-SCLC) model. With this model, we can quantify the SCLC parameters in different regimes of the J-V curves (ohmic, trap filling, and quadratic regions) associated with the charge carrier injection properties of the perovskite-based devices and map the trap filling inside of the semiconductor bandgap. Moreover, we simulated the influence of Fermi level position, temperature, trap position and trap temperature on the energetic dependencies of the trapped charge concentration (Supplementary Figs. S8–S12). The capabilities of the proposed A-SCLC model were presented on two perspectives organometal halide perovskite single crystals MAPbBr$_3$ and MAPbI$_3$ (see Supplementary Fig. S1). The data for evaluation were collected by measuring the J-V characteristics of Carbon/Perovskite/Carbon devices in dark and under illumination. In addition, we discussed the effect of thermodynamic Fermi level shift and different charge injection properties of the studied materials.

Results and discussion
Analysis of J-V curves
In the early works[56,57], A. Rose determined that the two requirements have to be fulfilled in order to observe space charge limited currents in low conducting materials: (i) at least one of the contact must be ohmic (i.e. the contact that provides an excess of carriers ready to enter the studied material) and (ii) the studied material has to be relatively free from trap states. The first requirement was fulfilled by contacting perovskites in sandwich-like (Supplementary Fig. S5) carbon contacts (e.g. C/MAPbBr$_3$/C), and the monocrystalline form of perovskites were used to ensure the high periodicity of the crystalline lattice and low trap concentration needed to fulfill the second requirement. Structural and optical analysis of the prepared materials are presented in Supplementary Figs. S3, S4.

The current-voltage characteristics of a semiconductor material with trap states can be divided into three regions: ohmic, trap filling and quadratic region. The electric properties of these materials can be analyzed by two current equations that describe the J-V curves of SCLC. First is Ohm's law describing the linear current dependence on applied bias voltage:

$$J = e\mu_0 p_f \frac{V}{L} \qquad (1)$$

where e is an elementary charge ($e = 1.602 \cdot 10^{-19}$ C), μ_0 is the microscopic mobility, p_f (n_f) is a concentration of free charge carriers (electrons or holes), L represents the thickness of the sample. The second equation is given by the combination of Poisson's equation and Ohm's law:

$$J = \varepsilon_0 \varepsilon_r \mu_0 \Theta (1-\gamma)(2-\gamma)^2 \frac{V^2}{L^3} \qquad (2)$$

where ε_0 is vacuum permittivity ($\varepsilon_0 = 8.854 \cdot 10^{-12}$ F m^{-1}), ε_r is relative permittivity (dielectric constant), Θ is the fraction of free (p_f) and total (p_s) charge carrier concentrations[45,53] in the material (i.e. $\Theta = p_f/p_s = p_f/(p_f + p_t)$, where p_t is a trapped charge concentration), and γ is inversely proportional to the logarithmic slope (m) of the current-voltage characteristic (i.e. $\gamma = 1/m = \mathrm{d} \ln V/\mathrm{d} \ln J$)[58,59]. The parameter theta Θ

and gamma γ can be used to identify different regions of the J-V curves. For instance, if the gamma equals one ($m = 1 \rightarrow \gamma = 1$), ohmic region occurs. If the injected charge accumulates in the semiconductor (i.e. space charge region), the slope of the J-V curve increases and γ takes on values between zero and one ($0 < \gamma < 1$). In the space charge region, we can observe two different situations: (i) the slope m approaches infinity ($m \rightarrow \infty \Rightarrow \gamma = 1$) for trap filled limit (TFL), and (ii) Mott–Gurney region for slope m equals two ($m = 2 \Rightarrow \gamma = 1/2$). If the latter is the case, then Eq. (2) transforms to Mott–Gurney law

$$J = \frac{9}{8} \varepsilon_0 \varepsilon_r \mu_0 \Theta \frac{V^2}{L^3} \qquad (3)$$

However, in some special cases, due to anomalies of charge transport (e.g. injection barrier), the slope m can be lower than one, in which case the current suddenly decreases in a forward biased scan. The parameter theta Θ equals one ($\Theta = 1$) in ohmic region when $p_t = 0$ as well as in Mott-Gurney region, where $p_s \approx p_f$ ($p_t \ll p_f$). In other regions of J-V curves theta takes on values between zero and one ($0 < \Theta < 1$). The full explanation of the model including different regions of the curves and graphical presentation of theta are described in Supplementary Information (see Supplementary Figs. S13–S15). All described relations are derived for hole-only devices.

Figure 1 illustrates the band diagrams of two studied perovskite-based devices (C/MAPbBr$_3$/C and C/MAPbI$_3$/C) before contact, after contact at zero bias voltage and after applied bias voltage (forward scan). Moreover, the figure illustrates the band bending caused by illumination and applied bias voltage. As evident, the Fermi level equilibrates after contacting, and bands in MAPbBr$_3$ and MAPbI$_3$ bend for 0.172 eV and 0.126 eV, respectively. The thermodynamic Fermi level changes due to the illumination causing additional bending (0.260 eV for MAPbBr$_3$ and 0.254 eV MAPbI$_3$). The energy difference between the thermodynamic Fermi level positions under dark and illuminated conditions is reffered to as the Fermi level shift.

Figure 2 shows the J-V characteristics of MAPbBr$_3$ and MAPbI$_3$ single crystals measured under dark (yellow dots) and under white LED illumination of 34 W m^{-2} (orange dots) in forward scan regime only with low voltage scan rate of 1 mV s^{-1}. Raw and average data plots are shown in Supplementary Information (see Supplementary Figs. S17, S18). Previous research suggests[53–55] that ion migration plays an important role in the hysteresis effect and shape of J-V curves. Hence, we carried out an extensive analysis to determine the mobilities and ion concentrations in our halide perovskite single crystals (for further information see Supplementary Fig. S16). Based on the analysis and comparison with DD simulation model we decided to proceed using simplified Eq. (3) to model the measured J-V curves (see Fig. 2 and Supplementary Figs. S17, S18).

To gain a better understanding of the current-voltage characteristics, we introduced the injection (solid line red) and, and the opposite, extraction model (dashed red line). The current density and voltage are plotted on a logarithmic scale. A detailed explanation of the applied models is presented in Supplementary Figs. S6, S7. The other two lines (i) dashed black line and (ii) solid black line correspond with the ohmic region ($m = 1$) and quadratic region ($m = 2$), respectively.

Both characteristics exhibit noise for small voltage (ohmic region) and a clear change after illumination. In the case of MAPbBr$_3$ the illumination causes 1 order of magnitude increase in photocurrent in the ohmic region, while the TFL regions exhibit little to no difference. The transition between ohmic and TFL region occurs at 0.5 V, followed by the transition from TFL to quadratic region at around 3 V. The dark and light current-voltage characteristics follow the proposed injection model, with no indication of the barrier behavior. However, both curves enter Mott–Gurney region at 10 V and 9 V, respectively. On the contrary, dark and light current voltage characteristics of MAPbI$_3$ differ in the measured range. The dark J-V clearly shows the barrier behavior (i.e. follows the extraction model), while the light J-V follows the injection model with two transitions: (i) ohmic to TFL at 0.5 V and (ii) TFL to quadratic region at 3 V. This curve enters the Mott-Gurney region at ~10 V. Moreover, the current passing through the MAPbI$_3$
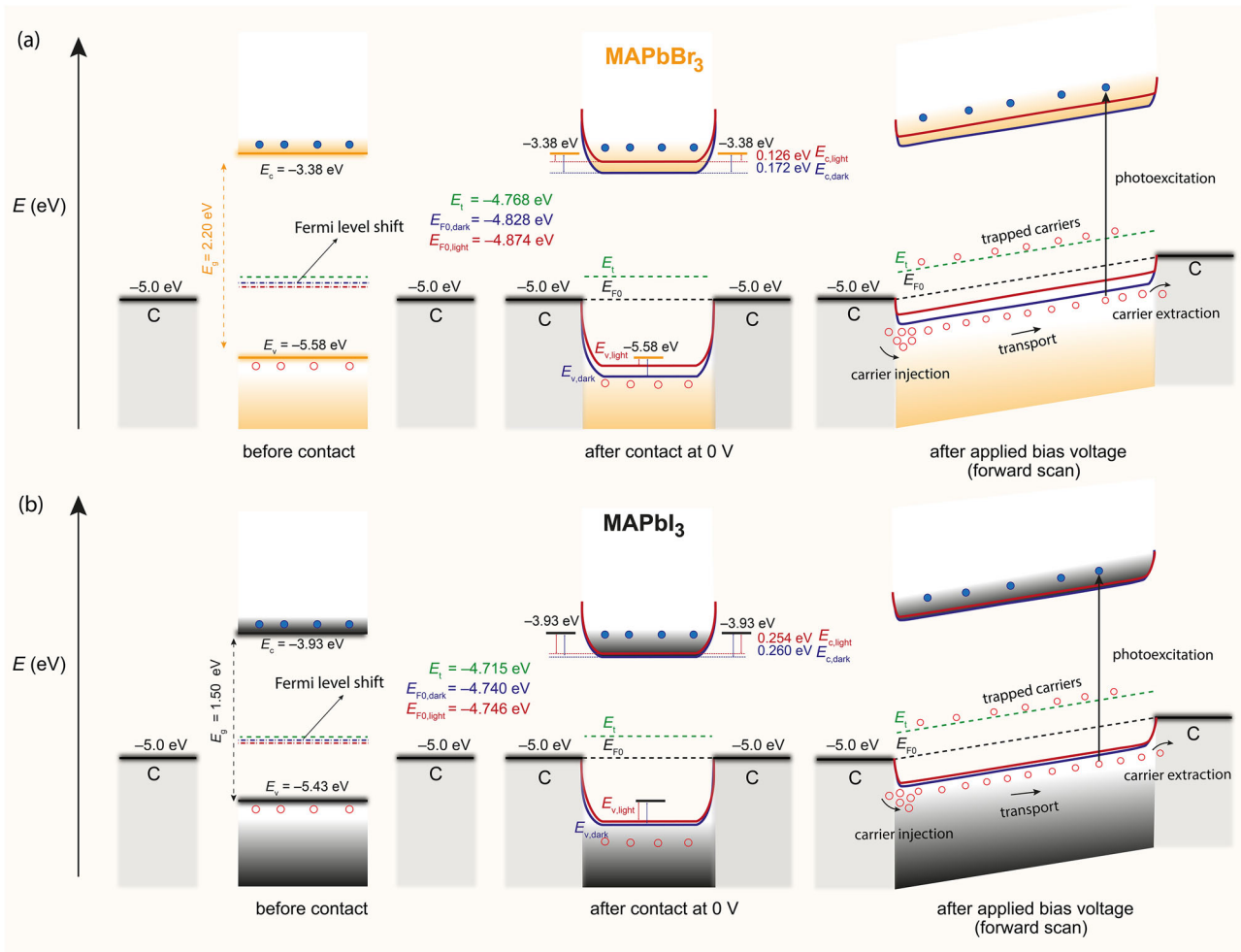
Fig. 1 | Graphical illustration of band diagrams under various measurement conditions. Band diagrams of **a** Carbon/MAPbBr$_3$/Carbon and **b** Carbon/MAPbI$_3$/Carbon devices before and after contact (at 0 V and in forward regime). The diagrams consist of several energies: valence band energy (E_v), conduction band energy (E_c), energy of trap state (E_t), thermodynamic Fermi level (E_{F0}). The positions of valence band energy ($E_{v,dark}$ and $E_{v,light}$), conduction band energy ($E_{c,dark}$ and $E_{c,light}$) and Fermi level ($E_{F0,dark}$ and $E_{F0,light}$) in dark and under illumination are clearly indicated.

single crystal increases by about 1.5 orders of magnitude after illumination. The conductivity (σ) of both materials was determined from Ohmic regions of dark J-V curves using the following formula $\sigma = \frac{L}{AR}$, where L is the crystal thickness, A is the active area (Supplementary Table S1), R is the resistance. The conductivity of MAPbBr$_3$ was calculated to be $(3.9 \pm 0.6) \times 10^{-11}$ S cm^{-1}, while that of MAPbI$_3$ was found to be $(2.6 \pm 0.4) \times 10^{-10}$ S cm^{-1}.

To the best of our knowledge, the previously reported models[44–49] apply the tangent fits to the defined regions (ohmic, TFL and Mott–Gurney) in dark current-voltage characteristics and determine the parameters such as V_{TFL}, concentrations of trapped charge carriers (p_t or n_t), and their mobilities (μ_p and μ_n). However, the information about the energy distribution and voltage dependance of the determined parameters remains unclear. In addition, the localization of the trap state is usually missing, which might raise the question whether the simple fit by tangent is sufficient to describe these materials. Especially if we take into account that the trap state can cause the quadratic slope in J-V characteristics, same as the Mott–Gurney region (see Model Simulations in Supplementary Information). Hence, we developed the advanced space charge limited current model (A-SCLC) to investigate the electrical properties of halide perovskite materials. The model itself is a successor of temperature-modulated SCLC model[60–64], previously published by our group and it can be applied not only to perovskites but to other semiconductor materials as well.

Determination of the charge carrier mobilities and concentrations

To determine the key parameters of semiconductor materials one must take into account the band diagram of the studied material and the contacts, as shown in Fig. 1 and Supplementary Fig. S6. With that being said, we developed a model consisting of two square root transport bands (conduction and valence band) and one monoenergetic trap state. Practically, the proposed model variates with five parameters: (i) microscopic mobility μ_0, (ii) density of the trap states N_t, (iii) energy position of the trap state E_t, (iv) trap temperature T_t, and (v) thermodynamic Fermi level position E_{F0} to fit the J-V characteristics and simultaneously fit the calculated parameters (effective mobility, concentration of free and trapped charge carriers, Fermi level shift, and parameter theta). A detailed description of the model used is described in Supplementary Note 1. Supplementary Table S2 presents all parameters used to build the model, while Supplementary Fig. S7 represents a scheme used to calculate and model the studied parameters (for better understanding, a guide to data analysis and modeling is also included and explained in Supplementary Note 2).

The first of the calculated parameters, the effective mobility[58,62,65] of the charge carriers, can be derived from Eq. (2)

$$\mu_{eff} = \mu_0 \Theta = \frac{L^3}{\varepsilon_0 \varepsilon_r (1-\gamma)(2-\gamma)^2} \frac{J}{V^2} \qquad (4)$$
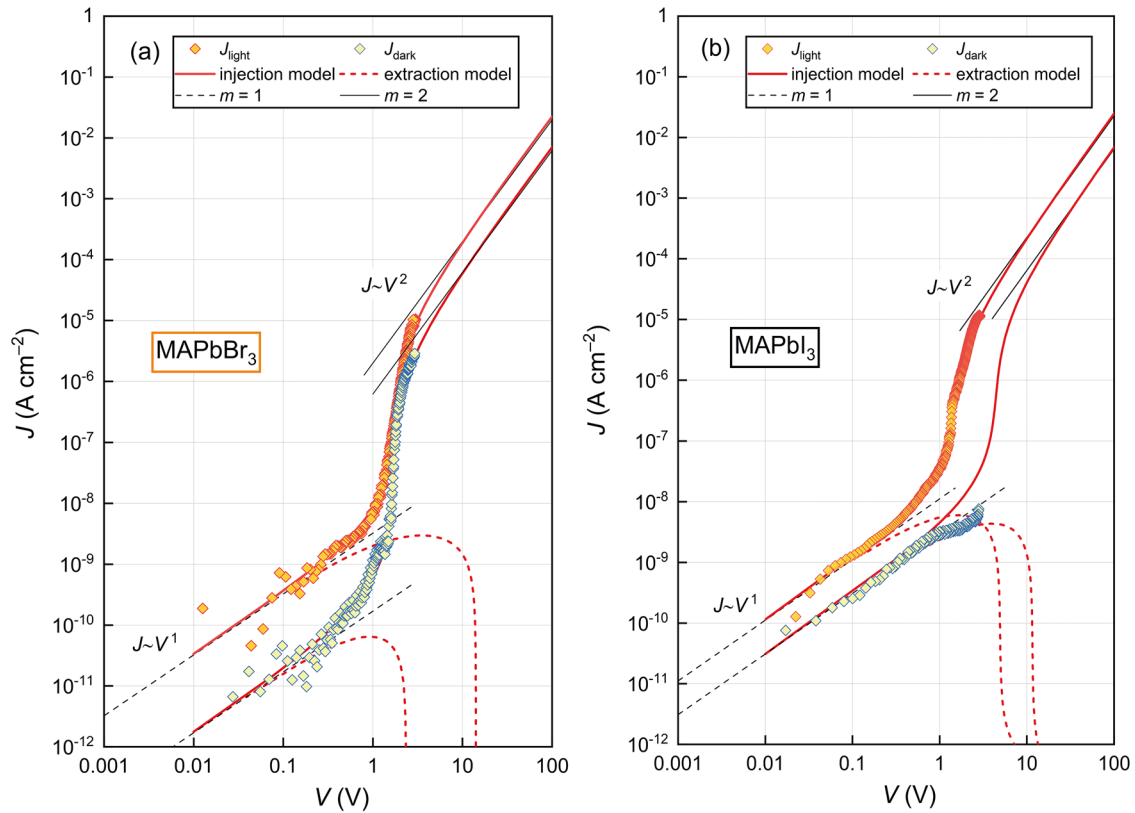
Fig. 2 | J-V curves under various experimental conditions. Experimental data and estimated models of current-voltage characteristics for **a** MAPbBr$_3$ and **b** MAPbI$_3$ perovskite single crystals in the dark (J_{dark}) and under illumination (J_{light}) fitted using injection and extraction model. Black dashed and solid lines represent linear and quadratic slopes (m) of J-V characteristics.
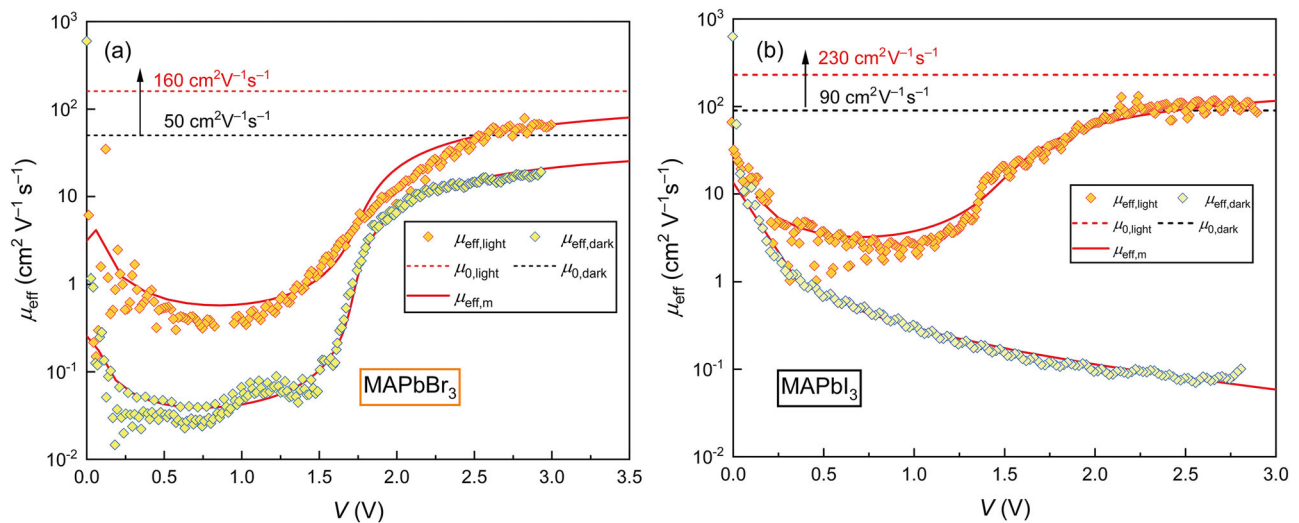
Fig. 3 | Tracking the change of effective mobility under applied bias voltage. Effective mobility (μ_{eff}) of **a** MAPbBr$_3$ and **b** MAPbI$_3$ perovskite single crystals, in the dark ($\mu_{eff,dark}$) and under illumination ($\mu_{eff,light}$). Red and black dashed lines represent estimated microscopic mobilities ($\mu_{0,dark}$ and $\mu_{0,light}$), while red solid lines represent models of effective mobility ($\mu_{eff,m}$).

Essentially, the microscopic mobility (μ_0) is the limiting case of effective mobility (μ_{eff}), which occurs when parameter Θ equals one (e.g. ohmic and Mott-Gurney regions). However, the trap states lower the effective mobility and thereby the magnitude of SCLC ($\Theta \leq 1$). Hence, to precisely determine the mobility, it is necessary to either measure J-V curves up to Mott-Gurney region, or to develop a model that can estimate at which voltage the device enters this region of current-voltage characteristics and then calculate the semiconductor's properties.

Figure 3 shows the dependence of effective mobility on the applied voltage under dark and light measurement conditions (experimental data), their models (solid red curves) and estimated microscopic mobility values (dashed lines). Interestingly, both dark and light effective mobility of MAPbBr$_3$ approaches the M-G region (i.e. effective mobility approaches the microscopic mobility), while in the case of MAPbI$_3$ only the light μ_{eff} follows the same trend. The dark μ_{eff} decreases with increasing voltage, reflecting the barrier behavior previously seen in the current-voltage characteristics. In

Table 1 | Summarized parameters for MAPbBr$_3$ and MAPbI$_3$ single crystals

	MAPbBr$_3$	MAPbI$_3$
E_c (eV)	–3.36	–3.93
E_v (eV)	–5.58	–5.43
$E_{F0,intrinsic}$ (eV)	–4.47	–4.68
E_g (eV)	2.20	1.50
$N_{t, dark}$ (cm^{-3})	3.03×10^{10}	4.60×10^{10}
$N_{t, light}$ (cm^{-3})	3.54×10^{10}	3.45×10^{10}
E_t (eV)	–4.768	–4.715
$T_{t, dark}$ (K)	8	40
$T_{t, light}$ (K)	40	95
$E_{F0,dark}$ (eV)	–4.828	–4.740
$E_{F0,light}$ (eV)	–4.874	–4.746
ΔE_{F0} (eV)	0.046	0.006
$\mu_{0,dark}$ (cm^{2}V^{-1}s^{-1})	50	90
$\mu_{0,light}$ (cm^{2}V^{-1}s^{-1})	160	230
$\mu_{0,light}/\mu_{0,dark}$	3.2	2.5
$p_{t,dark}$ (cm^{-3})	7.58×10^9	1.15×10^{10}
$p_{t,light}$ (cm^{-3})	8.84×10^9	8.63×10^9
n_{ions} (cm^{-3})	1.65×10^9	4.52×10^7
μ_{ions} (cm^{2}V^{-1}s^{-1})	4.25×10^{-5}	1.39×10^{-7}
T (K)	300	

our case, the microscopic mobility of MAPbI$_3$ under dark can be determined only from ohmic region. We note that such behavior was previously measured in MAPbI$_3$-based hole-only devices[48]. Estimated microscopic mobilities for both single crystals are presented in Table 1. The voltage dependence of Θ is shown in Supplementary Fig. S19.

Once microscopic mobility is estimated, we can calculate the concentration of free and trapped charge carriers (in our case holes), p_f and p_t using following relations

$$p_f = \frac{LJ}{e\mu_0 (2-\gamma) V} \qquad (5)$$

$$p_t = \frac{\varepsilon_0 \varepsilon_r (1-\gamma)(2-\gamma) V}{e L^2} \qquad (6)$$

Figure 4a, b shows voltage dependences of experimental p_f and p_t and their models for two studied crystals MAPbBr$_3$ and MAPbI$_3$, respectively. As evident, the illuminated MAPbBr$_3$ single crystal exhibits an increase of free carriers in ohmic region, while MAPbI$_3$ exhibits an increase in free charge carriers over the entire measurement range. These findings correlate with the J-V curves (Fig. 1). Moreover, the concentration of trapped charge carriers can also be plotted as a function of free charge carrier concentration and Fermi level (top and bottom axis in Fig. 4c, d). The model concentrations of free and trapped charge carriers were plotted for holes (solid p_{tm} and dashed p_{fm} red lines indicating positive charge) and for electrons (solid n_{tm} and dashed n_{fm} blue lines indicating negative charge). This representation of the modeled and calculated concentration gives a deeper understanding of the charge carrier transport mechanisms. Firstly, note that in the case of MAPbBr$_3$, the concentration of trapped charge follows the model of hole carriers (red line), while in MAPbI$_3$ only the points calculated from light J-V characteristics do so. This trend responds with injection behavior (i.e. ohmic and TFL region transition). A detailed explanation regarding the different regions of the J-V curves and their correlation with the p_t (p_f) and n_t (n_f) functions is shown in the model simulation (see

Supplementary Fig. S15). In addition, the saturated value of p_t (see Fig. 4c, d), that is the total concentration of trapped charge carriers, increases from 7.58×10^9 cm^{-3} (under dark) to 8.84×10^9 cm^{-3} (after illumination) for MAPbBr$_3$. In the case of MAPbI$_3$ we notice a different behavior under dark. Trapped charge carriers follow the trend of n_t instead of p_t. This could be related to a blocking mechanism at the injection contact causing extraction dominance and sudden decrease of free charge carriers (see Fig. 4d and Supplementary Fig. S22b, c). However, there is a change in concentration of trapped charge carriers from 1.15×10^{10} cm^{-3} under dark to 8.63×10^9 cm^{-3} after illumination.

Another interesting situation occurs at the point where concentration of trapped holes equals the concentration of free holes, $p_t \approx p_f$. Given that in this situation $\Theta = p_f/p_s = p_f/(p_t + p_f)$, we can deduce that $\mu_{eff} = \mu_0 \Theta = \mu_0/2$. Using the proposed model one can precisely determine where this situation occurs and test the modeling of the microscopic mobility.

Determination of quasi-Fermi level position

Fermi level position is another parameter that could be fitted using the A-SCLC model. To determine the position of the Fermi level, we must use the following equation

$$p_f = N_v e^{\left(-\frac{\Delta E_F}{k_B T}\right)} \qquad (7)$$

where N_v is the concentration of delocalized states in the valence band and ΔE_F is the Fermi level shift ($\Delta E_F = E_F - E_v$) relative to the position of valence band (as shown in Fig. 1). Figure 5a, b shows calculated dark and light Fermi level positions as well as the corresponding model curves for MAPbBr$_3$ and MAPbI$_3$. Again, we notice different trends in two-measured single crystals. Light and dark quasi-Fermi level of MAPbBr$_3$ moves closer to transport band with increasing voltage, which agrees with proposed injection mechanism and increase of the p_f. On the contrary, dark quasi-Fermi level of MAPbI$_3$ single crystal moves farther away from the transport band up to approx. 2 V, after which the Fermi level shows the opposite trend. This supports our earlier statement that the presence of injection barrier leads to dominance of extraction mechanisms and decrease of free charge carriers (see Fig. 4b).

However, the injection barrier is removed either with higher voltage (>2 V) or by illumination, as shown in Fig. 4b and Supplementary Fig. S23. Expectedly, we noticed a shift of thermodynamic Fermi level E_{F0} (E_F at 0 V) after illumination in both measured single crystals: from –4.828 eV to –4.874 eV ($\Delta E_{F0} = 0.046$ eV) in MAPbBr$_3$ and from –4.740 eV to –4.746 eV ($\Delta E_{F0} = 0.006$ eV) in MAPbI$_3$.

## Energy distributions of the studied parameters

Energy distributions of calculated p_t, p_f and model curves p_{tm}, p_{fm} (n_{tm}, n_{fm}) give in-depth information about the charge transport processes inside of the semiconductor's bandgap. Firstly, about the tendency of the carriers to move closer or further away from the transport band, and secondly about the quantity of the trapped (free) charge carrier concentrations. The model itself consists of two square root (approximately monoenergetic) transport bands (valence and conduction band) and one bi-exponential (approximately monoenergetic) trap states. All states are described with function $g(E)$, presented with a green dashed line in Fig. 6. Previous reports suggest that halide perovskite materials have significant defect tolerance[10,14–28]. Nevertheless, the trap states influence the charge transport and thus they cannot be neglected in the SCLC model. The effect of trap position and trap temperature on the p_{tm} and n_{fm} is presented in the Model Simulation section of Supplementary Information. As can be seen from this section, trap temperature does not significantly affect p_{tm} and p_{fm} for temperatures lower than the temperature of the experiment T (K), where $E_{F0} \approx E_t$. However, the position of thermodynamic Fermi level has the highest impact on the shape of p_{tm} and n_{tm}. Supplementary Fig. S8 shows three possible positions of the thermodynamic Fermi level relative to the trap position: (i) E_{F0} closer to
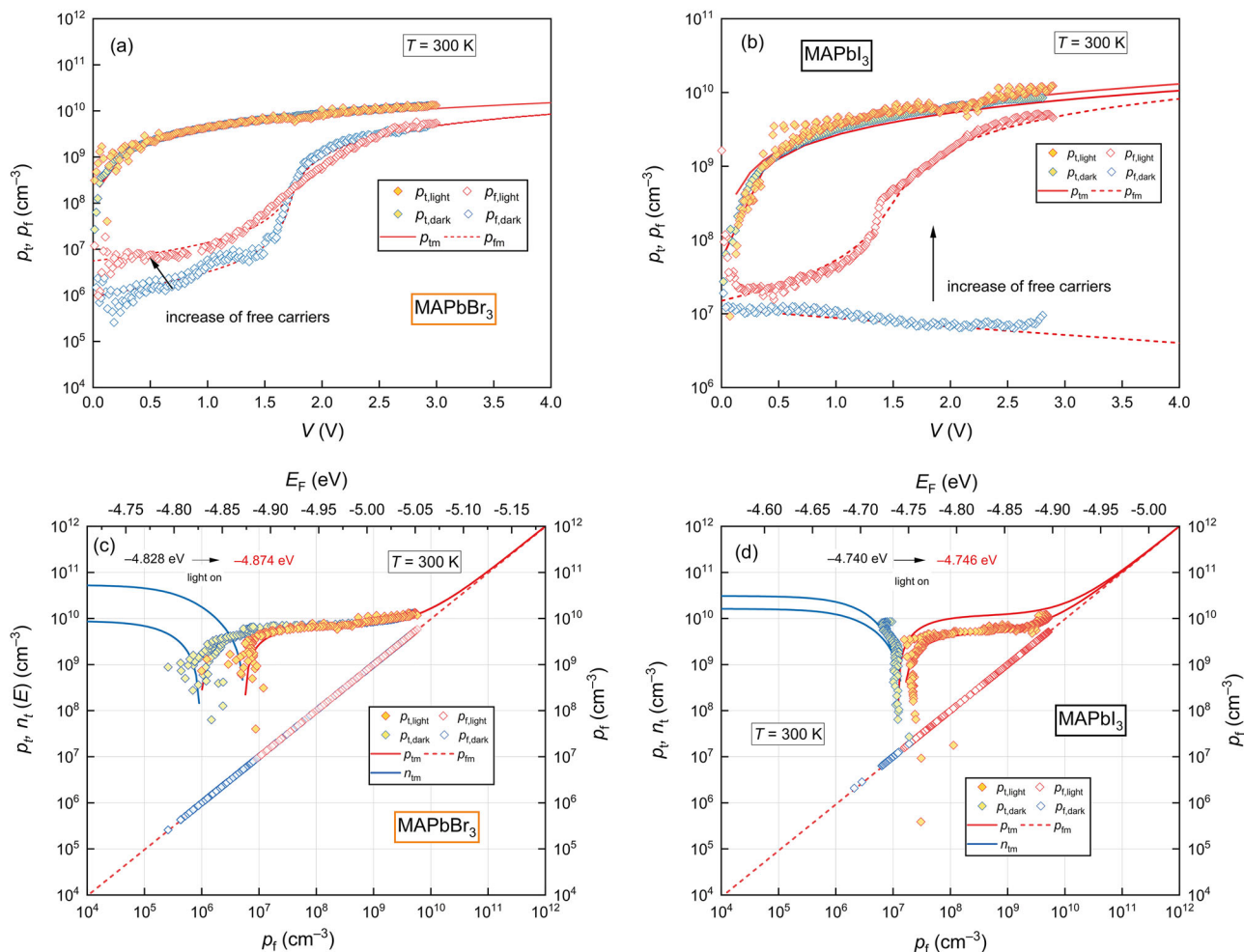
Fig. 4 | Change of carrier concentrations and their mapping using A-SCLC model. Voltage dependence of free (p_f) and trapped (p_t) charge carriers for **a** MAPbBr$_3$ and **b** MAPbI$_3$ and energy dependances of p_f and p_t for **c** MAPbBr$_3$ and

d MAPbI$_3$. The solid blue and red lines represent model curves (n_{tm} and p_{tm}) of trapped charge carriers. Red dashed line represents model curve of free charge carriers (p_{fm}).
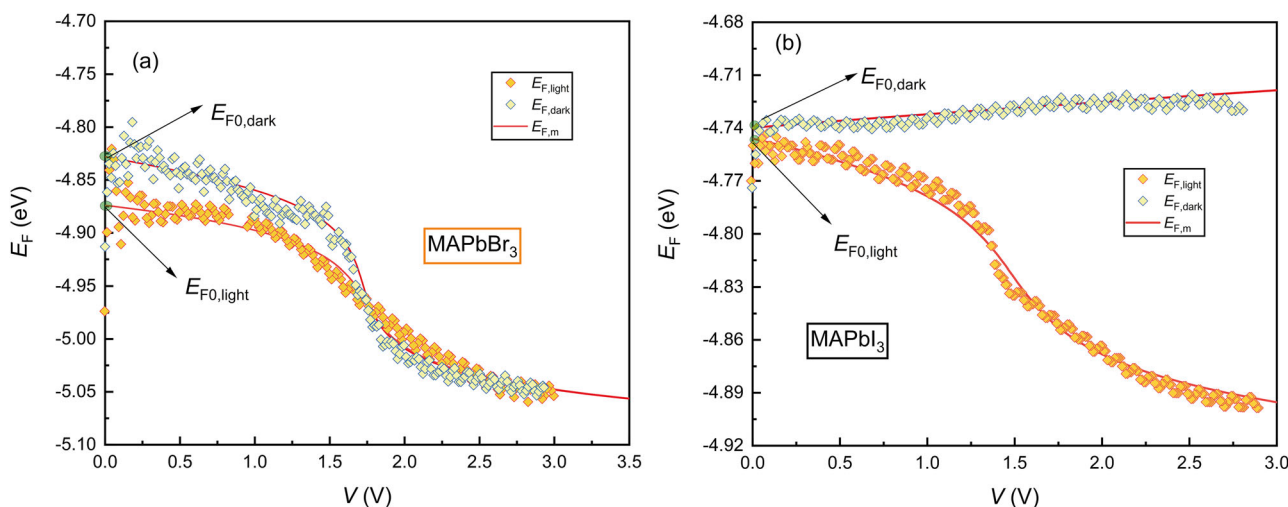
Fig. 5 | Effect of applied bias voltage on Fermi level position. Voltage dependence of Fermi level of **a** MAPbBr$_3$ and **b** MAPbI$_3$, in the dark ($E_{F,dark}$) and under illumination ($E_{F,light}$). The solid red line represents model of Fermi level energy

($E_{F,m}$). The thermodynamic Fermi level positions in the dark ($E_{F0,dark}$) and under illumination ($E_{F0,light}$) are indicated by black arrows.
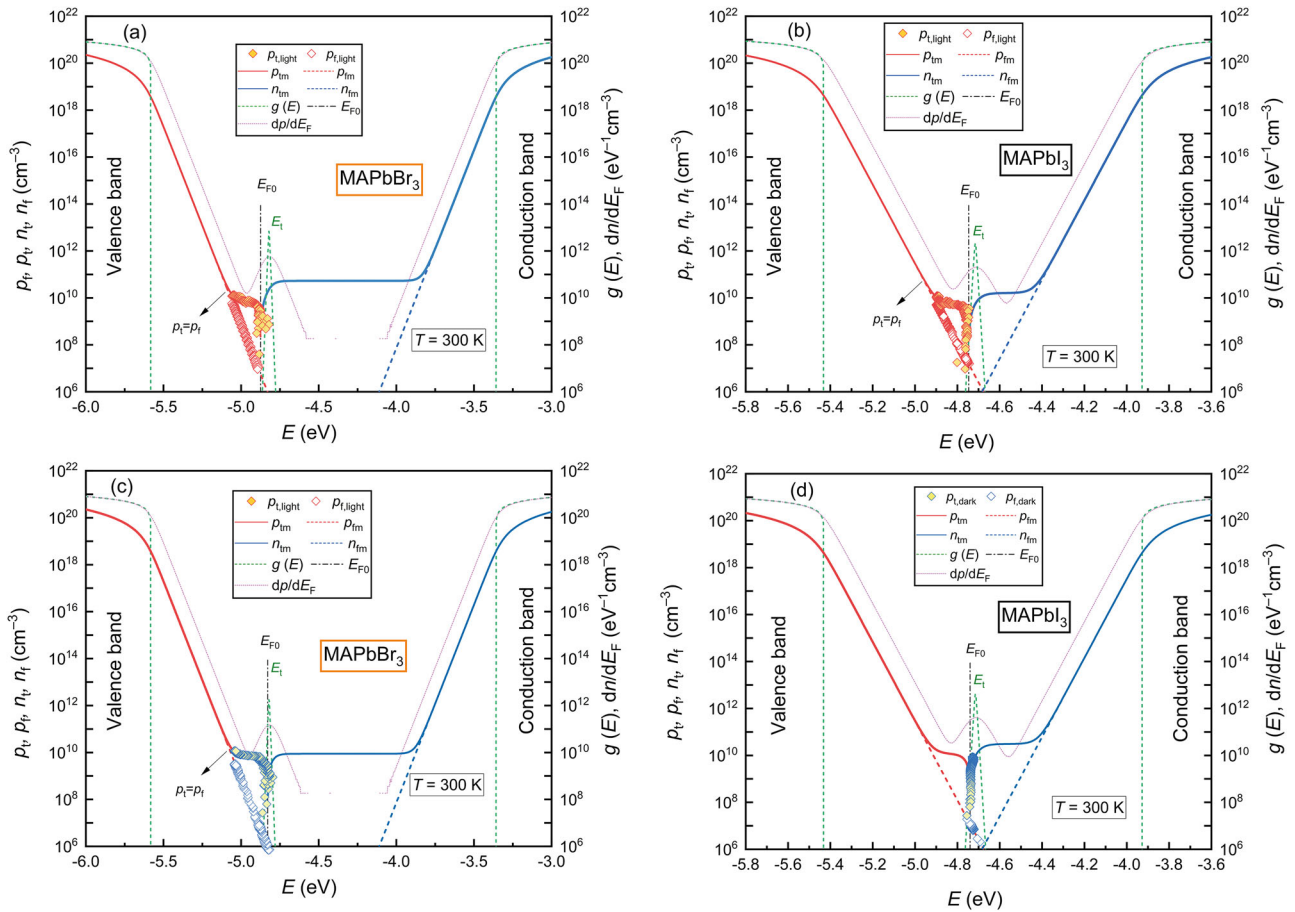
Fig. 6 | A-SCLC bandgap maps. Energy distribution of density of states $g(E)$ model (green dashed lines), modeled p_{tm} (p_{fm}) and n_{tm} (n_{fm}) curves (red and blue lines), the concentration increment dp_{tm}/dE (dashed pink lines) and experimental data points p_t and p_f plotted for light (**a**, **b**) and dark (**c**, **d**) measurements performed on MAPbBr$_3$ and MAPbI$_3$, respectively. The trap state (E_t) position (green dashed line) and the Fermi level (E_{F0}) position (dashed black line) are clearly indicated.

the conduction band, (ii) E_{F0} in the position of the trap state, and (iii) E_{F0} closer to the valence band. Furthermore, the proposed A-SCLC model can distinguish minor changes in the concentration of trapped charge carriers and free carriers in the bandgap of semiconductor materials. The traditional SCLC models (tangent fit of J-V regions) usually do not interpret these changes.

It our case, both MAPbBr$_3$ and MAPbI$_3$-based devices have thermodynamic Fermi level position closer to the valence band, $E_{F0} < E_t$ (i.e. deep trap state for holes, see Table 1). Figure 6 shows the discussed trends of hole concentrations in the wider energy range. In addition, the increment of charge carrier concentration (dp_t/dE) is plotted to better demonstrate the increase/decrease of the trapped holes. The effect of temperature on p_{tm} (n_{tm}) and dp_{tm}/dE is simulated in Supplementary Figs. S10, S11.

Figure 6 also reveals the change of the free and trapped holes in the bandgap of the two studied halide perovskite materials. As mentioned above, the trapped holes in MAPbBr$_3$ follow the p_{tm}, which corresponds with injection mechanism in C/MAPbBr$_3$/C (Figs. 4a, c and 6a, c) both under dark and after illumination (i.e. p_t increases with increasing voltage and p_{tm} fits p_t). On the contrary, the hole injection mechanism is negligible in C/MAPbI$_3$/C device under the dark condition, and the hole extraction dominates, leading the device into barrier-like mode (Fig. 2b). As a result of that, we notice a low concentration of free charge carriers under dark (7×10^6 cm^{-3}), which stays almost constant up to 2.5 V (Fig. 4b, d). Under higher voltage, the hole injection surpasses the extraction, and the p_f concentration increases (the injection barrier is overcome). Figures 4b and 6d suggest that barrier can be overcome with illumination as well. Thus, after illumination we notice that the p_t follows p_{tm} and that concentration of p_t significantly increases after illumination. To get a better understanding of

illumination effect on MAPbBr$_3$ and MAPbI$_3$ we compared all parameters determined by the A-SCLC model in Table 1.

The described model is applicable not only to halide perovskites but to other semiconductor materials as well. Nevertheless, there are certain criteria that must be considered before evaluating the measured current-voltage characteristics. Firstly, the mapping of trap state is possible only for lower temperatures (see Supplementary Fig. S10). If temperatures surpass the critical temperature, the trap is not visible in the p_{tm} and n_{tm}. Secondly, in materials such as halide perovskites, where diffusion of ions, polarization effects, reactions between ions and electrodes, influence the J-V curves, the measurements have to be carried out in steady state regime. In addition, it is noteworthy to mention that 2-electrode configuration can suffer from surface current. Thus, we recommend others to use ring-guard electrode configuration, described by Almora et al.[66] prior to application of our A-SCLC model.

Conclusions
Herein, we report a comprehensive analysis of the current-voltage characteristics of two commonly studied perovskite materials: methylammonium lead bromide (MAPbBr$_3$) and methylammonium lead iodide (MAPbI$_3$) single crystals. Using advanced space charge limited current (A-SCLC) model we determined the key semiconductor properties (microscopic mobility, thermodynamic Fermi level, trap position and concentration of majority charge carriers) in two carbon/perovskite/carbon devices under dark and after white LED illumination (all results are summarized in Table 1). Two different behaviors can be seen from the measured and modeled parameters. The C/MAPbBr$_3$/C device showed clear injection properties, where the concentration of free and trapped holes (i.e. majority

charge carriers) increased after applied bias voltage, both under dark and after illumination. On the contrary, C/MAPbI$_3$/C showed presence of injection barrier that altered the shape of the *J-V* curve under dark measurement conditions. This could be caused by interface defects or by self-doping of MAPbI$_3$ due to the presence of intrinsic defect state (i.e. ion vacancies, interstitials etc.)[67]. As shown in our results, the injection barrier can be overcome with higher voltage (>2 V) and after illumination. The proposed advanced- SCLC model presented in this work is a guide for detailed analysis of current-voltage characteristics, applicable to a broad range of semiconductor materials.

Methods
Chemicals and reagents
Methylammonium bromide (6876-37-5, ≥99%, CH$_3$NH$_3$Br, MABr), methylammonium iodide (14965-49-2, ≥99%, CH$_3$NH$_3$I, MAI), lead (II) bromide (10031-22-8, 99% PbBr$_2$), lead (II) iodide (10101-63-0, 99% PbI$_2$), N,N-dimethylformamide (68-12-2, 99% DMF), γ-butyrolactone (96-48-0, 99% GBL), and propylene carbonate (108-32-7, 99% PC) were purchased from Merck (Sigma-Aldrich). All chemicals were used as received without further purification.

Preparation of the MAPbBr$_3$ and MAPbI$_3$ single crystals
Organometal halide perovskite single crystals (MAPbBr$_3$ and MAPbI$_3$) were synthesized using inverse temperature crystallization (ITC) method. Firstly, the equimolar ratios of perovskite precursors MABr (MAI) and PbBr$_2$ (PbI$_2$) were dissolved in polar aprotic solvents: bromides in DMF and iodides in GBL/PC (65%:35% v/v). As prepared, 1 ml perovskite solutions were then stirred for 3 h at 25 °C; subsequently, they were filtered using 0.45 μm polytetrafluoroethylene (PTFE) filters. Those solutions were later poured in 4 ml vials and placed into silicon oil bath to ensure the uniform temperature distribution. The whole set-up was then placed onto the SuperNuova+ (Thermo Scientific™) hotplate with PT1000 temperature probe and heated from 25 °C to 80 °C. As a result, the desired millimeter sized, MAPbBr$_3$ and MAPbI$_3$ single crystals were obtained (see Supplementary Figs. S1, S2).

Structural characterization
The crystalline structure of the prepared samples was determined using an X-ray diffractometer (XRD) equipped with the Cu Kα X-ray tubes. The single crystal X-ray diffraction (SC-XRD) measurements were performed on an XtaLAB Synergy-I diffractometer with a HyPix3000 hybrid pixel array detector and microfocused PhotonJet-I X-ray source (Cu Kα). The data integration was done using CrysAlisPro 1.171.40.82a software. The XRD patterns for MAPbBr$_3$ and MAPbI$_3$ single crystals are shown in Supplementary Fig. S3.

Optical characterization
Microscopic photos of the prepared single crystals were captured using a Hirox RH-2000 digital microscope. The UV-VIS absorbance spectra were recorded at room temperature using a Varian Cary 50 UV-VIS Spectrophotometer operating in the 200–800 nm region with a step of 1 nm. Samples were excited by 380 nm nanosecond LED source from the front side at an angle of 45°. Absorption and photoluminescence spectra of the prepared materials are shown in Supplementary Fig. S4.

Device fabrication
C/MAPbBr$_3$/C and C/MAPbI$_3$/C devices were prepared by depositing the perovskite grade carbon paste (DM-CAP-4703S, Dycotec Materials) at the two opposite facets of the prepared bulk single crystals as shown in Supplementary Fig. S5. Subsequently, the samples were encapsulated with Ossila epoxy resin to minimize the potential degradation due to the exposure to oxygen and moisture. This encapsulation was performed in a glovebox under an inert atmosphere (<1 ppm O$_2$).

A-SCLC measurements
Advanced space charge limited current spectroscopy was performed using the Keithley Electrometer/High-resistance meter (model 6571B) at constant temperature (300 K) in vacuum/isolation chamber. The dark and light (34 W m^{-2} white LED reflector LR4605.5dDG-WFL) current-voltage (*J-V*) characteristics were measured in forward scan only in sandwich configuration Carbon/Perovskite/Carbon (see Supplementary Fig. S5), with a voltage scan rate of 1 mV s^{-1}. The temperature was regulated and measured using a Lauda ECO Silver RE 415 and a Digit NanoVolt/MicroOhm meter (Agilent 34420 A thermocouple type K).

Impedance spectroscopy
Analysis of ion mobilities and concentrations was performed using Solartron SI 1260 Impedance/Gain-Phase Analyzer with Solartron Dielectric Interface 1296. Measurements were carried out at ambient temperature under dark (at 0 V voltage bias and 3V-biased), see Supplementary Fig. S16.

Data availability
The data that support the findings of this study are available from the corresponding authors upon reasonable request.

References
1. Kojima, A., Teshima, K., Shirai, Y. & Miyasaka, T. Organometal halide perovskites as visible-light sensitizers for photovoltaic cells. *J. Am. Chem. Soc.* **131**, 6050–6051 (2009).
2. Liang, Z. et al. Homogenizing out-of-plane cation composition in perovskite solar cells. *Nature* **624**, 557–563 (2023).
3. De Wolf, S. et al. Organometallic halide perovskites: sharp optical absorption edge and its relation to photovoltaic performance. *J. Phys. Chem. Lett.* **5**, 1035–1039 (2014).
4. Jiang, Y., Green, M. A., Sheng, R. & Ho-Baillie, A. Room temperature optical properties of organic–inorganic lead halide perovskites. *Sol. Energy Mater. Sol. Cells* **137**, 253–257 (2015).
5. MENG, G. et al. Recent progress of halide perovskite radiation detector materials. *J. Inorganic Mater.* https://doi.org/10.15541/jim20190394 (2020).
6. Sutton, R. J. et al. Bandgap-tunable cesium lead halide perovskites with high thermal stability for efficient solar cells. *Adv. Energy Mater.* **6**, 1502458 (2016)
7. Kulkarni, S. A. et al. Band-gap tuning of lead halide perovskites using a sequential deposition process. *J. Mater. Chem. A* **2**, 9221–9225 (2014).
8. Gao, H. et al. Bandgap engineering of single-crystalline perovskite arrays for high-performance photodetectors. *Adv. Functional Mater.* **28**, https://doi.org/10.1002/adfm.201804349 (2018).
9. Wehrenfennig, C., Liu, M., Snaith, H. J., Johnston, M. B. & Herz, L. M. Homogeneous emission line broadening in the organo lead halide perovskite CH$_3$NH$_3$PbI$_{3-x}$Cl$_x$. *J. Phys. Chem. Lett.* **5**, 1300–1306 (2014).
10. Xing, G. et al. Long-range balanced electron- and hole-transport lengths in organic-inorganic CH$_3$NH$_3$PbI$_3$. *Science* **342**, 344–347 (2013).
11. Herz, L. M. Charge-carrier mobilities in metal halide perovskites: fundamental mechanisms and limits. *ACS Energy Lett.* **2**, 1539–1548 (2017).
12. Lim, J. et al. Elucidating the long-range charge carrier mobility in metal halide perovskite thin films. *Energy Environ. Sci.* **12**, 169–176 (2019).
13. Iftikhar, F. J. et al. Structural and optoelectronic properties of hybrid halide perovskites for solar cells. *Org. Electronics* **91**, https://doi.org/10.1016/j.orgel.2021.106077 (2021).
14. Liu, Y. et al. Ligand assisted growth of perovskite single crystals with low defect density. *Nat. Commun.* **12**, https://doi.org/10.1038/s41467-021-21934-6 (2021).

15. Feng, Y. et al. Low defects density $CsPbBr_3$ single crystals grown by an additive assisted method for gamma-ray detection. *J. Mater. Chem. C.* **8**, 11360–11368 (2020).

16. Xia, J., Sohail, M. & Nazeeruddin, M. K. Efficient and stable perovskite solar cells by tailoring of interfaces. *Adv. Mater.* **35**, https://doi.org/10.1002/adma.202211324 (2023).

17. Lee, D.-K. & Park, N.-G. Additive engineering for highly efficient and stable perovskite solar cells. *Appl. Phys. Rev.* **10**, https://doi.org/10.1063/5.0097704 (2023).

18. Zhang, Z. et al. Suppression of phase segregation in wide-bandgap perovskites with thiocyanate ions for perovskite/organic tandems with 25.06% efficiency. *Nat. Energy* https://doi.org/10.1038/s41560-024-01491-0.

19. Gaonkar, H. et al. Thermally stable, efficient, vapor deposited inorganic perovskite solar cells. *ACS Appl. Energy Mater.* **3**, 3497–3503 (2020).

20. Jošt, M., Kegelmann, L., Korte, L. & Albrecht, S. Monolithic perovskite tandem solar cells: a review of the present status and advanced characterization methods toward 30% efficiency. *Adv. Energy Mater.* **10**, https://doi.org/10.1002/aenm.201904102 (2020).

21. Chen, M. et al. High-efficiency lead-free wide band gap perovskite solar cells via guanidinium bromide incorporation. *ACS Appl. Energy Mater.* **4**, 5615–5624 (2021).

22. Ma, Y., Zhao, X., Xu, X., Wei, W. & Shen, L. Ultralow dark current and high on–off ratio of perovskite photodetectors enabled by 3D/2D/3D heterostructures unipolar barrier. *Appl. Phys. Lett.* **123**, https://doi.org/10.1063/5.0179174 (2023).

23. Liu, D. et al. Metal halide perovskite nanocrystals: application in high-performance photodetectors. *Mater. Adv.* **2**, 856–879 (2021).

24. Feng, X. et al. Spray-coated perovskite hemispherical photodetector featuring narrow-band and wide-angle imaging. *Nat. Commun.* **13**, https://doi.org/10.1038/s41467-022-33934-1 (2022).

25. Song, J., Zhou, Y., Padture, N. P. & Huey, B. D. Anomalous 3D nanoscale photoconduction in hybrid perovskite semiconductors revealed by tomographic atomic force microscopy. *Nat. Commun.* **11**, https://doi.org/10.1038/s41467-020-17012-y (2020) .

26. Lee, K. J. et al. Gigantic suppression of recombination rate in 3D lead-halide perovskites for enhanced photodetector performance. *Nat. Photonics* **17**, 236–243 (2023).

27. She, X.-J. et al. A solvent-based surface cleaning and passivation technique for suppressing ionic defects in high-mobility perovskite field-effect transistors. *Nat. Electron.* **3**, 694–703 (2020).

28. Matsushima, T. et al. Large metal halide perovskite crystals for field-effect transistor applications. *Appl. Phys. Lett.* **115**, https://doi.org/10.1063/1.5116411 (2019).

29. Sulaman, M. et al. Hybrid nanocomposites of all-inorganic halide perovskites with polymers for high-performance field-effect-transistor-based photodetectors: an experimental and simulation Study. *Adv. Mater. Interfaces* **9** https://doi.org/10.1002/admi.202200017 (2022).

30. Pininti, A. R., Ball, J. M., Albaqami, M. D., Petrozza, A. & Caironi, M. Time-dependent field effect in three-dimensional lead-halide perovskite semiconductor thin films. *ACS Appl. Energy Mater.* **4**, 10603–10609 (2021).

31. Yang, D. et al. Germanium-lead perovskite light-emitting diodes. *Nat. Commun.* **12**, https://doi.org/10.1038/s41467-021-24616-5 (2021).

32. Liu, X.-K. et al. Metal halide perovskites for light-emitting diodes. *Nat. Mater.* **20**, 10–21 (2021).

33. Yin, W. et al. Multidentate ligand polyethylenimine enables bright color-saturated blue light-emitting diodes based on $CsPbBr_3$ nanoplatelets. *ACS Energy Lett.* **6**, 477–484 (2021).

34. Liu, H. et al. Efficient and stable blue light emitting diodes based on $CsPbBr_3$ nanoplatelets with surface passivation by a multifunctional organic sulfate. *Adv. Energy Mater.* **13**, https://doi.org/10.1002/aenm.202201605 (2023).

35. John, R. A. et al. Reconfigurable halide perovskite nanocrystal memristors for neuromorphic computing. *Nat. Commun.* **13**, https://doi.org/10.1038/s41467-022-29727-1 (2022).

36. Berruet, M. et al. Physical model for the current–voltage hysteresis and impedance of halide perovskite memristors. *ACS Energy Lett.* **7**, 1214–1222 (2022).

37. Zhang, N. et al. All-optical control of lead halide perovskite microlasers. *Nat. Commun.* **10**, https://doi.org/10.1038/s41467-019-09876-6 (2019).

38. Guo, P. et al. Laser-generated nanocrystals in perovskite: universal embedding of ligand-free and sub-10 nm nanocrystals in solution-processed metal halide perovskite films for effectively modulated optoelectronic performance. *Adv. Energy Mater.* **9**, https://doi.org/10.1002/aenm.201901341 (2019).

39. Qin, C. et al. Stable room-temperature continuous-wave lasing in quasi-2D perovskite films. *Nature* **585**, 53–57 (2020).

40. Guo, J. et al. Ultrashort laser pulse doubling by metal-halide perovskite multiple quantum wells. *Nat. Commun.* **11**, https://doi.org/10.1038/s41467-020-17096-6 (2020).

41. Knop, O., Wasylishen, R. E., White, M. A., Cameron, T. S. & Oort, M. J. M. V. Alkylammonium lead halides. Part 2. $CH_3NH_3PbX_3$ (X = Cl, Br, I) perovskites: cuboctahedral halide cages with isotropic cation reorientation. *Can. J. Chem.* **68**, 412–422 (1990).

42. Zhou, Z., Pang, S., Liu, Z., Xu, H. & Cui, G. Interface engineering for high-performance perovskite hybrid solar cells. *J. Mater. Chem. A* **3**, 19205–19217 (2015).

43. Rao, H. -S., Li, W. -G., Chen, B. -X., Kuang, D. -B. & Su, C. -Y. In situ growth of 120 cm^2 $CH_3NH_3PbBr_3$ perovskite crystal film on FTO glass for narrowband-photodetectors. *Adv. Mater.* **29**, https://doi.org/10.1002/adma.201602639 (2017).

44. Liu, Y. et al. A 1300 mm^2 ultrahigh-performance digital imaging assembly using high-quality perovskite single crystals. *Adv. Mater.* **30**, https://doi.org/10.1002/adma.201707314 (2018).

45. Saidaminov, M. I. et al. Planar-integrated single-crystalline perovskite photodetectors. *Nat. Commun.* **6**, https://doi.org/10.1038/ncomms9724 (2015).

46. Shi, D. et al. Low trap-state density and long carrier diffusion in organolead trihalide perovskite single crystals. *Science* **347**, 519–522 (2015).

47. Saidaminov, M. I. et al. High-quality bulk hybrid perovskite single crystals within minutes by inverse temperature crystallization. *Nat. Commun.* **6**, https://doi.org/10.1038/ncomms8586 (2015).

48. Dong, Q. et al. Electron-hole diffusion lengths 175 μm in solution-grown CH3NH3PbI3 Single Crystals. *Science* **347**, 967–970 (2015).

49. Huang, Y. et al. A-site cation engineering for highly efficient MAPbI3 single-crystal X-ray detector. *Angew. Chem. Int. Ed.* **58**, 17834–17842 (2019).

50. Almora, O. et al. Capacitive dark currents, hysteresis, and electrode polarization in lead halide perovskite solar cells. *J. Phys. Chem. Lett.* **6**, 1645–1652 (2015).

51. McGovern, L., Futscher, M. H., Muscarella, L. A. & Ehrler, B. Understanding the stability of MAPbBr3 versus MAPbI3: suppression of methylammonium migration and reduction of halide migration. *J. Phys. Chem. Lett.* **11**, 7127–7132 (2020).

52. Futscher, M. H. et al. Quantification of ion migration in CH3NH3PbI3 perovskite solar cells by transient capacitance measurements. *Mater. Horiz.* **6**, 1497–1503 (2019).

53. Duijnstee, E. A. et al. Toward understanding space-charge limited current measurements on metal halide perovskites. *ACS Energy Lett.* **5**, 376–384 (2020).

54. Le Corre, V. M. et al. Revealing charge carrier mobility and defect densities in metal halide perovskites via space-charge-limited current measurements. *ACS Energy Lett.* **6**, 1087–1094 (2021).

55. Sajedi Alvar, M., Blom, P. W. M. & Wetzelaer, G.-J. A. H. Space-charge-limited electron and hole currents in hybrid organic-inorganic

perovskites. *Nat. Commun.* **11**, https://doi.org/10.1038/s41467-020-17868-0 (2020).

56. Rose, A. Space-charge-limited currents in solids. *Phys. Rev.* **97**, 1538–1544 (1955).

57. Rose, A. & Lampert, M. A. Photoconductor performance, space-charge currents, and the steady-state fermi level. *Phys. Rev.* **113**, 1227–1235 (1959).

58. Stöckmann, F. An exact evaluation of steady-state space-charge-limited currents for arbitrary trap distributions. *Phys. Status Solidi* **64**, 475–483 (1981).

59. Tan, S. et al. Inorganic ammonium halide additive strategy for highly efficient and stable CsPbI$_3$ perovskite solar cells. *Adv. Functional Mater.* **31**, https://doi.org/10.1002/adfm.202010813 (2021).

60. Schauer, F., Nespurek, S. & Zmeskal, O. The bulk trap spectroscopy of solids by temperature-modulated space-charge-limited currents (TMSCLC): Application to real crystalline and amorphous semiconductors. *J. Phys. C Solid State Phys.* **19**, 7231–7246 (1986).

61. Zmeskal, O., Schauer, F. & Nespurek, S. The bulk trap spectroscopy of solids by temperature-modulated space-charge-limited currents (TMSCLC) in the steady state. *J. Phys. C Solid State Phys.* **18**, 1873–1884 (1985).

62. Nešpůrek, S., Zmeškal, O. & Sworakowski, J. Space-charge-limited currents in organic films: some open problems. *Thin Solid Films* **516**, 8949–8962 (2008).

63. Pospisil, J. et al. Density of bulk trap states of hybrid lead halide perovskite single crystals: temperature modulated space-charge-limited-currents. *Sci. Rep.* **9**, https://doi.org/10.1038/s41598-019-40139-y (2019).

64. Zia, Q. et al. Impact of Low-Temperature Seed-Assisted Growth on the Structural and Optoelectronic Properties of MAPbBr$_3$ Single Crystals. *Chem. Mater*. **35**, 5458–5467 (2023).

65. Robertson, J. H. Electrical transport in solids, with particular reference to organic semiconductors by K. C. Kao and W. Hwang. *Acta Crystallogr. Sect. B Struct. Crystallogr. Cryst. Chem.* **38**, 350–350 (1982).

66. Almora, O. et al. Surface versus bulk currents and ionic space-charge effects in CsPbBr 3 single crystals. *J. Phys. Chem. Lett.* **13**, 3824–3830 (2022).

67. Frolova, L. A., Dremova, N. N. & Troshin, P. A. The chemical origin of the p-type and n-type doping effects in the hybrid methylammonium–lead iodide (MAPbI$_3$) perovskite solar cells. *Chem. Commun.* **51**, 14917–14920 (2015).

Acknowledgements

Author contributions

Stevan Gavranovic: writing – original draft, synthesis of single crystals, model simulations, optical characterization, data curation. Jan Pospisil: writing – review and editing, methodology, structural and electrical characterization, modeling of current-voltage characteristics. Oldrich Zmeskal: development of space charge limited current model, formal analysis. Martin Weiter: supervision, conceptualization.

Competing interests

The authors declare that they have no known competing financial interests or personal relationships that could have appeared to influence the work reported in this paper. The funders had no role in the design of the study; in the collection, analysis, or interpretation of data; in the writing of the manuscript, or in the decision to publish the results.

Additional information

Supplementary information The online version contains supplementary material available at https://doi.org/10.1038/s42005-025-02202-1.

Correspondence and requests for materials should be addressed to Stevan Gavranovic or Jan Pospisil.

Peer review information *Communications Physics* thanks Vincent Le Corre, Atsushi Wakamiya and the other, anonymous, reviewer(s) for their contribution to the peer review of this work. A peer review file is available.

Reprints and permissions information is available at http://www.nature.com/reprints

Publisher's note Springer Nature remains neutral with regard to jurisdictional claims in published maps and institutional affiliations.